Optica Applicata, Vol. XXXII, No. 1–2, 2002

Simulation of thermal properties of proton-implanted top-surface-emitting lasers. II. Results and discussion

Włodzimierz Nakwaski

Institute of Physics, Technical University of Łódź, ul. Wólczańska 219, 93–005 Łódź, Poland.
Center for High Technology Materials, University of New Mexico, Albuquerque, NM, USA.

Paweł Maćkowiak

Institute of Physics, Technical University of Łódź, ul. Wólczańska 219, 93–005 Łódź, Poland.

Marek Osiński

Center for High Technology Materials, University of New Mexico, Albuquerque, NM, USA.

The comprehensive analytical thermal model of proton-implanted top-surface-emitting lasers (PITSELs) presented in the first part of the paper is applied to study thermal characteristics of GaAs/AlGaAs/AlAs devices with the active diameter of 35 μm. In the model, both the voltage saturation above the lasing threshold and the temperature increase in the laser heat sink are taken into account. Our results show that intense heating occurs at high pumping currents which is followed by a distinct thermal waveguiding effect within the central part of laser active regions. Long tails of radial temperature distributions, on the other hand, will result in severe thermal crosstalk if integration of these devices into densely packed two-dimensional arrays were to be attempted. Minimization of electrical series resistance is shown to be very important for improving the device performance.

1. Introduction

A GaAs/AlGaAs/AlAs proton-implanted top-surface-emitting laser (PITSEL) is still one of the most popular designs (see, *e.g.*, [1]–[8]) of vertical-cavity surface-emitting lasers (VCSELs) because of its relatively simple manufacturing, low series electrical resistance [9], and wavelength compatibility (and associated cascadability) with GaAs-based photothyristors and phototransistors [10]. In the first part [11] of the present paper, a comprehensive analytical thermal model of PITSEL has been developed and the solution algorithm has been described. In this part, the above model is applied to simulate an operation of a typical 35-μm PITSEL design. In successive sections of the paper, the laser structure under consideration is described (Sec. 2), the

device parameters are given (Sec. 3), the temperature increase in the laser heat sink is analysed (Sec. 4) and numerical results are presented together with their discussion (Sec. 5) which is followed by conclusions (Sec. 6).

2. Laser structure

Figure 1 shows a schematic view of a GaAs/AlGaAs/AlAs PITSEL. For simplicity, the device is assumed to be cylindrically symmetric. The specific device structure under consideration is similar to the first historical VCSEL design for which the room-temperature continuous-wave (CW) operation was reported [9]. This design

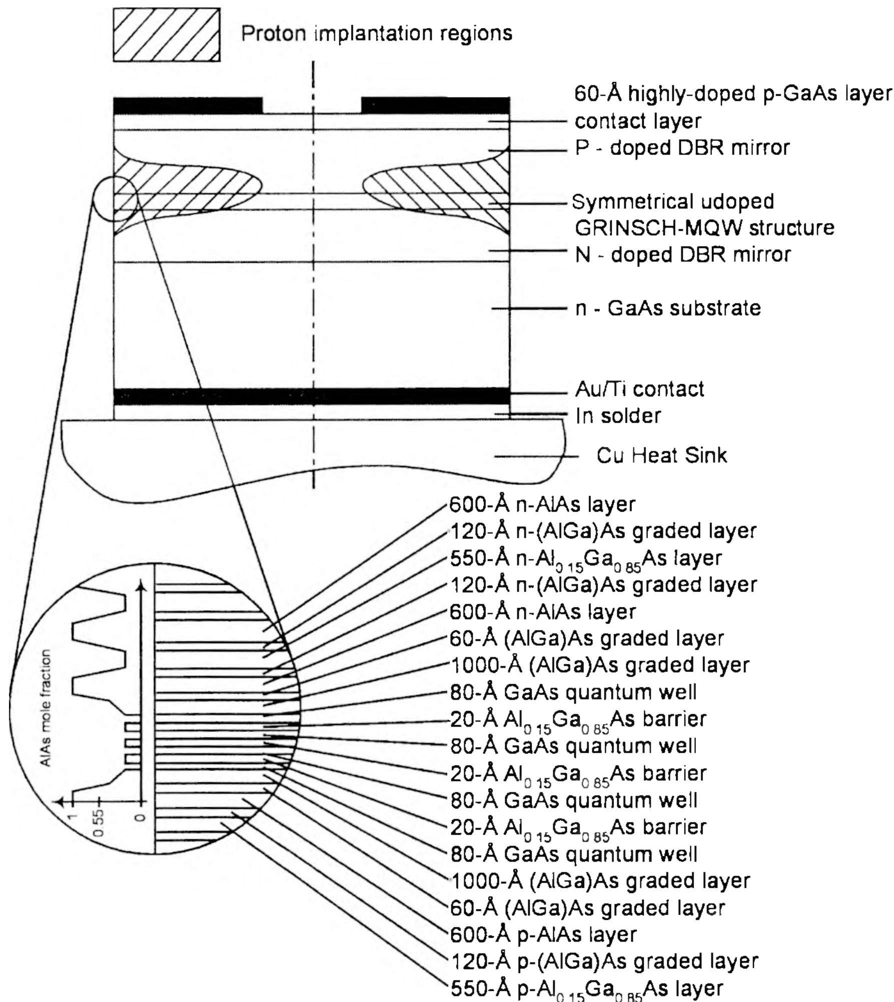

Fig. 1. Schematic structure of a proton-implanted top-surface-emitting GaAs/AlGaAs/AlAs vertical-cavity semiconductor laser (PITSEL) mounted p-side up. Active-region neighbourhood is enlarged.

remains still a typical PITSEL construction. Its graded-index separate-confinement -heterostructure (GRINSCH) active region consists of several GaAs/AlGaAs quantum wells and is sandwiched between two multilayer AlGaAs/AlAs Bragg reflectors. Lateral boundaries of the active region are defined by highly resistive proton-implanted regions. The device is mounted p-side up. In order to reduce series resistance, all interfaces in the distributed-Bragg-reflector (DBR) sections are linearly graded. In addition, the p-contact layer is very highly doped, facilitating the radial current spreading. Taking also into account the fact that the voltage drop in the DBR layers is much larger than variations of the junction voltage, the current injection into the active region is assumed to be homogeneous.

3. Device parameters

The device under consideration has the active-region diameter $D_A = 35\ \mu m$, which corresponds to the most efficient PITSEL reported in [9]. The external structure diameter D_s is taken as 500 μm. The N-type Bragg reflector consists of 43.5 half-wave periods of $Al_{0.15}Ga_{0.85}As$/AlAs layers, while the P-type mirror consists of 24 periods of the same layers. The laser is mounted on a copper heat-sink of much larger dimensions. From the observed CW threshold current at room temperature (RT) $I_{th,CW} = 10.2$ mA, we deduce the RT pulsed threshold $I_{th,P} = 9.9$ mA, corresponding to the active-region temperature equal to that of the ambient. To do this, we use familiar Arrhenius-type relation for the temperature dependence of the threshold

$$I_{th,CW}(300\ K + \Delta T) = I_{th,CW}(300\ K)\exp\left(\frac{\Delta T}{T_0}\right). \tag{1}$$

Note that $I_{th,CW}$ (300 K) corresponds to the threshold in a laser whose RT active-region temperature is 300 K, which is equivalent to the RT pulsed threshold. The T_0 parameter ($T_0 = 210$ K), measured for similar devices, is taken from [12].

Contrary to edge-emitting diode lasers, in the case of vertical-cavity surface-emitting lasers considered in this paper, T_0 parameters depends on a spectral location of the mode wavelength with respect to the laser gain spectrum [13]. Therefore for very similar VCSEL designs, T_0 value may be very different depending on seemingly insignificant differences in their constructions. Also for the same VCSEL device, its value depends strongly on ambient temperatures: it may be equal to zero or even negative. Therefore T_0 should be carefully determined for the temperature range and the laser design under consideration. The above $T_0 = 210$ K value taken from [12] for a specified (although very similar to that considered in this paper) VCSEL design and room temperature should be here regarded only as an example.

Unless otherwise stated, the differential series resistance of the device at threshold is taken as $R_{s,0} = 33\ \Omega$, and the corresponding threshold voltage $U_{th}(R_{s,0}) = 2.0$ V. The temperature dependence of the voltage drop U_{pn} at the p-n junction is a direct consequence of the assumed diode current-voltage relation

$$I = I_s \exp(\beta U_{pn}) \tag{2}$$

where I_s is the reverse saturation current, and the diode parameter β is given by:

$$\beta = \frac{e}{m k_B T}. \tag{3}$$

Here, k_B is the Boltzmann constant and m is the diode quality factor ($m \approx 2$ for GaAs/AlGaAs junctions [14], [15]). The reverse saturation current density was assumed to be equal to 6×10^{-9} A/cm^2.

In our calculations, saturation of the voltage drop at the p-n junction above the lasing threshold [16], [17] is taken into account. It does not simply mean that U_{pn} is taken as constant above threshold, because an increase in the pumping current is followed by an increase in the active-region temperature, which results in an increase in the threshold current. Therefore, for a given value of an pumping current, the saturated value of the voltage drop at the p-n junction corresponds to an actual active-region temperature increase which is included in the model.

The current dependence of the external differential quantum efficiency η_d is found from the experimental light-current characteristic given for the device under consideration in Fig. 2d in [9]. A value of the internal quantum efficiency η_{int} is then determined indirectly from η_d, taking into account all radiation losses for given temperature distribution, including the effect of multiple reflections

$$\eta_{int} = \eta_d \left[1 + \sum_i (\alpha_i d_i) \frac{1 - R_T R_B \exp\left[-2\sum_i (\alpha_i d_i)\right]}{1 - R_T} \right] \tag{4}$$

where R_T and R_B stand for the top and bottom, respectively, reflection coefficients, α_i is the absorption coefficient of the i-th layer material (mainly accounting for free-carrier absorption) and d_i is the thickness of the i-th layer under consideration. Both summations should be carried out over all layers of the DBR mirrors and the GRINSCH structure.

Reflection coefficients of the top (R_T) and the bottom (R_B) DBR mirrors were determined using the approach proposed in [18], which gives R_T = 99.80% and R_B = 99.99%.

In our caculations, the compositionally-dependent thermal conductivity k of $Al_xGa_{1-x}As$ is assumed to vary with temperature in the same way as in the case of GaAs [19]

$$k(x, T) = k(x, 300\ \mathrm{K}) \left(\frac{300\ \mathrm{K}}{T}\right)^{5/4} \tag{5}$$

where the temperature T is to be expressed in Kelvins, and the RT thermal conductivity is given by [20]

$$k(x, 300\ \mathrm{K}) = \frac{0.44}{1 + 12.70x - 13.22x^2}, \quad \left[\frac{\mathrm{W}}{\mathrm{cmK}}\right]. \tag{6}$$

For linearly graded $Al_xGa_{1-x}As$ layers, effective thermal conductivities are determined by integrating Eq. (6). For the above layers with $x \in [0.15, 1.00]$, $x \in [0.15, 0.55]$ and $x \in [0.55, 1.00]$, this gives average thermal conductivities of 0.1750 W/cmK, 0.1227 W/cmK, and 0.2160 W/cmK, respectively.

We assume gold (0.1 μm) and tin (0.1 μm) contact layers of thermal conductivities 3.15 W/cmK and 0.666 W/cmK, respectively, and a 2-μm indium-solder layer of thermal conductivity 0.817 W/cmK. The copper heat-sink is assumed to have a conductivity of 3.98 W/cmK. All values of thermal conductivities for metallic layers are taken from [21].

All the $Al_{0.15}Ga_{0.85}As$ layers are assumed to have a doping concentration in the range from 1×10^{18} cm^{-3} to 5×10^{18} cm^{-3}. For these concentrations, the RT value of mobility of the majority carriers in the N-type $Al_{0.15}Ga_{0.85}As$ layers is assumed to be constant and equal to 1250 cm^2/Vs [22], whereas for the P-type $Al_{0.15}Ga_{0.85}As$ layers, it is assumed to change linearly from 130 cm^2/Vs (for P = 1×10^{18} cm^{-3}) to 75 cm^2/Vs (for P = 5×10^{18} cm^{-3}) [23], [24]. The AlAs layers are assumed to have a doping concentration in the range from 1×10^{18} cm^{-3} to 1×10^{19} cm^{-3}. Their RT mobility of majority carriers is for the N-type AlAs again assumed to be constant and equal to 60 cm^2/Vs [25], whereas for the P-type AlAs the mobility is changing linearly from 100 cm^2/Vs (for 1×10^{18} cm^{-3}) to 30 cm^2/Vs (for 1×10^{19} cm^{-3}) [26].

In the case of the N-type and P-type linearly graded $Al_xGa_{1-x}As$ layers, their RT electrical resistivities were found to be 6.1 times [27] and 1.65 times [28], respectively, higher than those of corresponding $Al_{0.15}Ga_{0.85}As$ layers. For nominally undoped linearly graded $Al_xGa_{1-x}As$ layers in the GRINSCH structure, residual average doping concentrations of 5×10^{17} cm^{-3} and 1×10^{17} cm^{-3} are assumed for layers with an AlAs mole fraction changing from 1.00 to 0.55 and from 0.55 to 0.15, respectively [29]. Their electrical resistivities are found to be 17 times and 3.6 times, respectively, higher than that of $Al_{0.15}Ga_{0.85}As$ [27].

For all the N-type layers and the nominally undoped layers, relative temperature dependence of electrical resistivities is assumed to follow the experimental data reported in [27]. For the P-type $Al_{0.15}Ga_{0.85}As$, AlAs and linearly graded layers, on the other hand, their relative temperature dependences of electrical resistivities are assumed to be proportional to $T^{0.58}$, to $T^{0.23}$, and to $T^{0.40}$, respectively, on the basis of experimental results reported in [28].

4. Temperature increase in the heat sink

For determination of the temperature increase ΔT_{HS} in the heat sink, we need the value of an effective radius r_{eff} of the area through which a uniform heat flux density may be assumed to enter the heat sink. We detemine this value using approach proposed in

[30], *i.e.*, we find the radius r_{eff} of a uniform heat flux which gives exactly the same average temperature increase in the heat sink as a real nonuniform heat flux. This procedure leads us to the following expression [30]:

$$r_{eff} = \left(\pi k_c \frac{\partial R_{TH}}{\partial d_c}\right)^{-1/2} \tag{7}$$

where R_{TH} is the thermal resistance of the entire device, and k_c and d_c are the thermal conductivity and the tickness of the tin contact layer.

For a uniform heat flow from the circle of diameter D_{eff} (= $2r_{eff}$) into a finite heat sink of a diameter D_{HS} and a thickness t_{HS}, the thermal resistance R_{HS} of the heat sink can be found using the formula reported in [31]

$$R_{HS} = R_{HS,1D}\left[1 + \left(\frac{\pi D_{HS}^2}{8 D_{eff} t_{HS}}\right)\left(1 - \frac{D_{eff}}{D_{HS}}\right)^{3/2}\right] \tag{8}$$

where $R_{HS,1D}$ is the thermal resistance of a one-dimensional heat flow, *i.e.*,

$$R_{HS,1D} = \frac{4 t_{HS}}{\pi D_{HS}^2 k_{HS}} \tag{9}$$

with k_{HS} denoting the thermal conductivity of the heat-sink material (for copper, k_{HS} = 398 W/cmK). Note that Eq. (8) reduces to Eq. (9) when $D_{eff} = D_{HS}$.

The temperature increase in the heat sink is determined from a simple formula

$$\Delta T_{HS} = Q_T R_{HS} \tag{10}$$

where Q_T (in Watts) is a total power of heat generation within the laser chip. The above approach enables us to discuss the impact of thermal conductivity and dimensions of the heat sink on thermal properties of PITSEL. In this work, the external heat-sink diameter D_{HS} is taken as 5 mm and its thickness t_{HS} as 2 mm.

5. Numerical results

Figure 2 shows the pumping current dependence of radial temperature profiles in the mid-plane of the active region calculated for a 35-μm PITSEL operating at room temperature. Note that the CW threshold current for this device is 10.2 mA, hence, the lowest profile in Fig. 2 shows the temperature profile just above threshold. Superlinear increase in the temperature at the centre of the active region ($r = 0$) in response to increased pumping current can be clearly seen. Consequently, the temperature profile becomes increasingly inhomogeneous, with a large temperature step between the centre ($r = 0$) and the edge ($r = r_A$) of the active region. This results in creation of a strong thermal waveguide with the refractive index step as large as 1.4×10^{-2} at

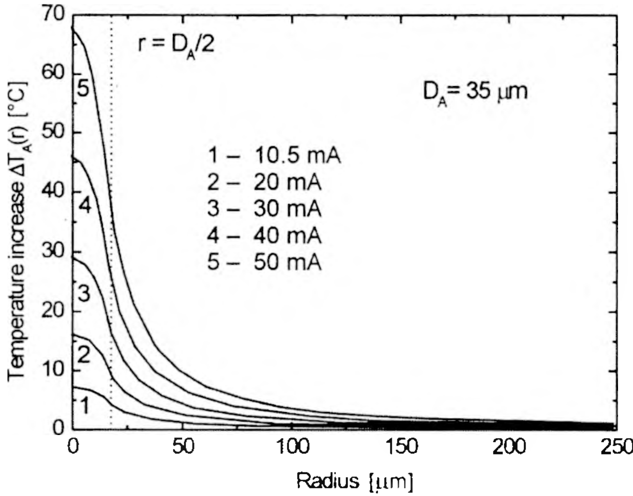

Fig. 2. Radial profiles of the active-region temperature increase $\Delta T_A(r)$ over the ambient temperature (300 K) for various CW pumping currents in a GaAs/AlGaAs/AlAs PITSEL with D_A = 35 μm.

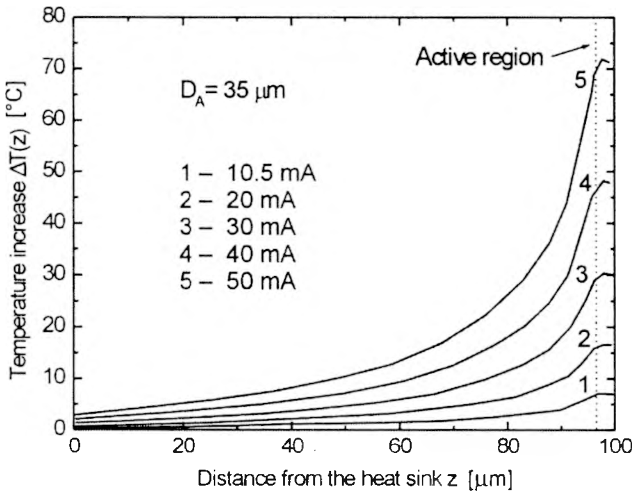

Fig. 3. Axial (r = 0) temperature profiles $\Delta T(z)$ for the same CW pumping conditions as those in Fig. 2.

I = 50 mA, which corresponds to an index step that would have been obtained if the active region were surrounded at room temperature by $Al_{0.02}Ga_{0.98}As$ rather than GaAs. On the other hand, since the slope dT/dr is a measure of the lateral heat flow, it is evident that the importance of 2D heat flow increases with the pumping current. In the same instance, a long tail of the temperature profile develops. This would result in a strong thermal crosstalk if these devices were to be integrated into densely packed 2D arrays, for which temperature increases originating from even the most distant emitters should be added [32].

Figure 3 shows axial temperature profiles calculated for the same pumping currents as the radial profiles presented in Fig. 2. The profiles exhibit a distinct maximum in the middle of the P-type DBR mirror which is a consequence of assumed localization of the corresponding flat heat source. The real temperature profile is of course somewhat smoother around this place. Nevertheless, the temperature profiles shown in Fig. 3 clearly confirm importance of at least one heat source located outside the active region, *i.e.* the P-type mirror heating.

Relative contributions of three major heat sources to the temperature profiles in the mid-plane of the active region are shown in Figs. 4 and 5, respectively, for two values of the pumping current, *i.e.*, $I = 1.5I_{th,p}$ and $I = 3.5I_{th,p}$. In both cases, the active -region heating appears to be the dominant heat source but for higher pumping current its dominance over the P-type mirror heating becomes much lower and eventually the P-type mirror heating dominates (Fig. 6). The situation reverses again near the thermal runaway limit, where we observe an accelerated increase in a relative importance of the active-layer heating (Fig. 7). This is caused by nonlinear processes inducing mainly a rapid increase in nonradiative recombination.

Figure 8 illustrates the current dependence of PITSEL thermal resistance R_{TH} defined as the ratio of the average active-region temperature increase $\Delta T_{A,\,av}$ and the total power Q_T of all heat sources in the device. Although R_{TH} is often treated as a constant parameter [33]–[35], it is clear that due to nonlinear processes it is a function of the pumping current. In addition to the experimentally realized device with $R_{s,0} = 33\ \Omega$ (curve 2), we also consider hypothetical devices with lower (curve 1) or larger (curves 3 and 4) series resistances. Corresponding threshold voltages are readjusted using the following equation:

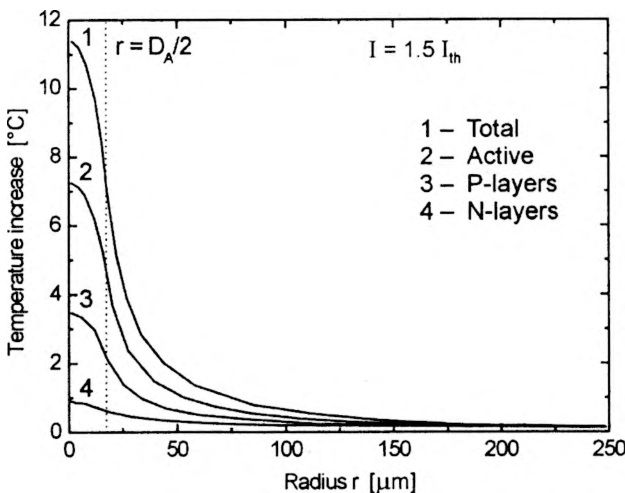

Fig. 4. Radial profiles of the partial active-region temperature increases associated with three major heat sources and the cumulative profile of $\Delta T_A(r)$ for the CW pumping current equal to 150% of the pulsed threshold value.

$$U_{th}(R_s) = U_0 + [U_{th}(R_{s,0}) - U_0]\frac{R_s}{R_{s,0}} \tag{11}$$

where U_0 is the voltage corresponding to the intersection of the linear part of the I–V characteristic above the lasing threshold with the voltage axis (*i.e.*, at $I = 0$). No variation of pulsed threshold current with R_s is assumed to take place. The CW

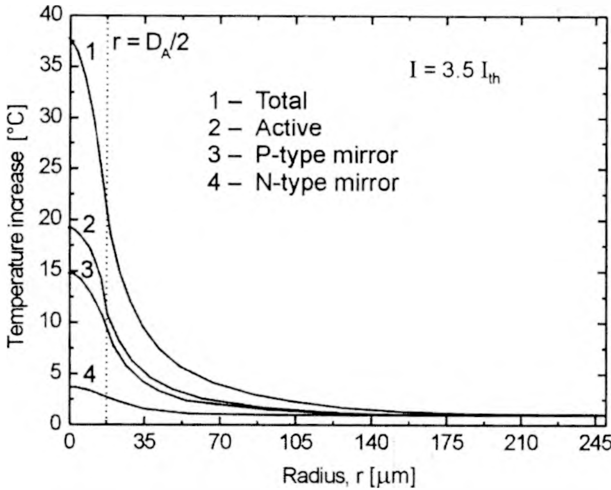

Fig. 5. Radial profiles of the partial active-region temperature increases associated with three major heat sources and the cumulative profile of $\Delta T_A(r)$ for the CW pumping current equal to 350% of the pulsed threshold value.

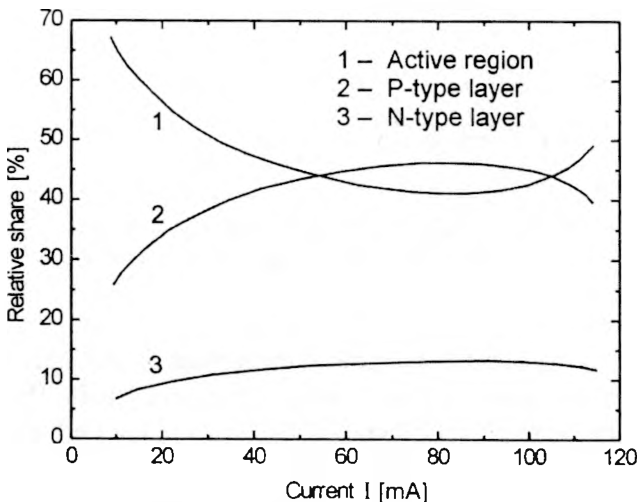

Fig. 6. Relative share of three major heat sources in a 35-μm-diameter PITSEL as a function of the pumping current.

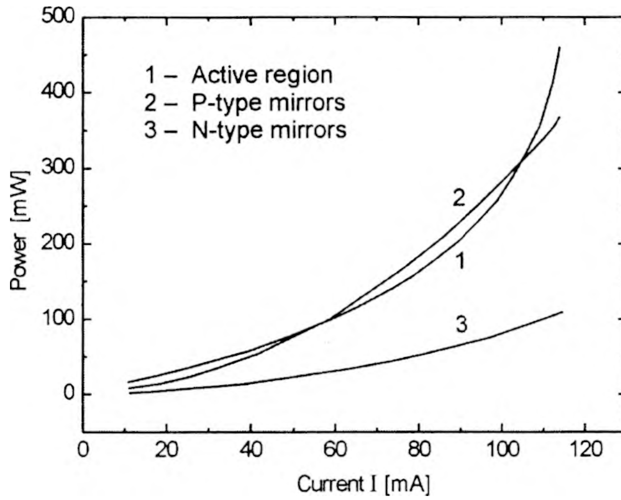

Fig.7. Yield of three major heat sources in a 35-μm-diameter PITSEL as a function of the pumping current.

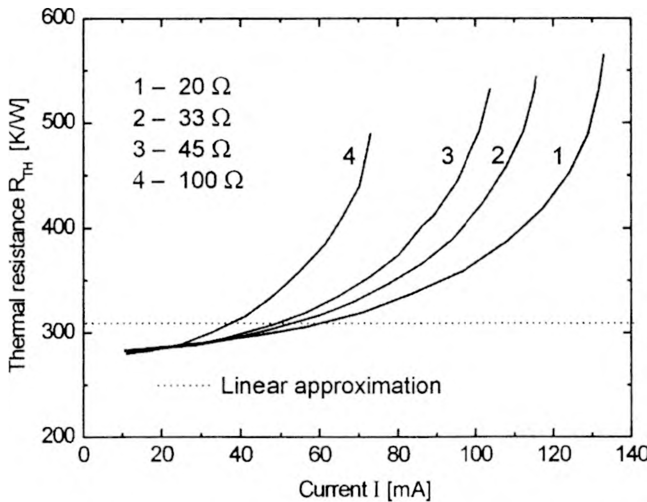

Fig. 8. Pumping-current dependence of thermal resistance R_{TH} for 35-μm-diameter GaAs/AlGaAs/AlAs PITSELs with various electrical series resistances. Dotted line: linear approximation [31]. Curve 2 corresponds to the device reported in [9].

threshold, however, does depend on R_s due to changing temperature of the active region, although for the devices considered here these changes are very small. The horizontal dotted line represents the thermal resistance calculated using the uniform cylinder model [31]. It is clear that this simplified model represents a reasonable approximation only in the linear regime, near the lasing threshold.

Effect of the series electrical resistance on the average temperature increase of the active region $\Delta T_{A,av}$, used in the calculation of the thermal resistance R_{TH}, is illustrated

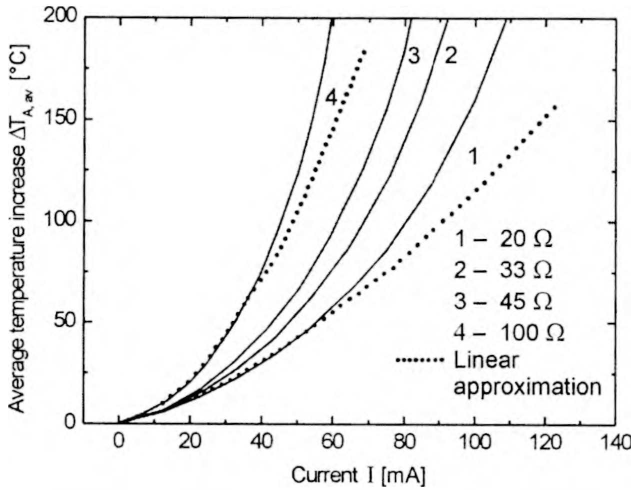

Fig. 9. Pumping-current dependence of the average active-region temperature increase $\Delta T_{A,\mathrm{av}}$ in a 35-μm-diameter GaAs/AlGaAs/AlAs PITSEL. Dotted lines: linear approximation [31]. Curve 2 corresponds to the device reported in [9].

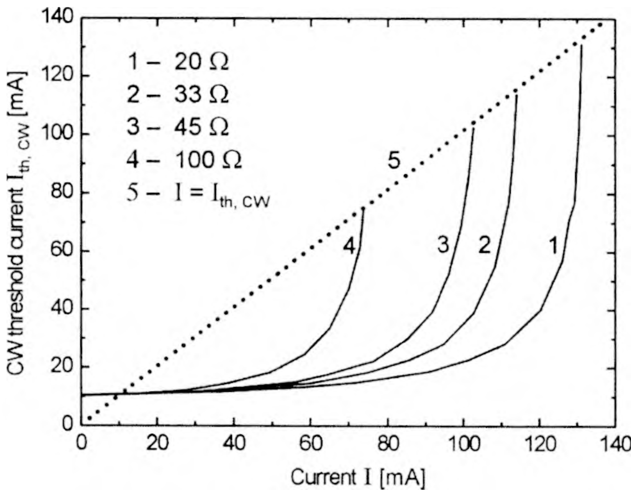

Fig. 10. Graph of CW threshold current variation with the pumping current 35-μm-diameter GaAs/AlGaAs/AlAs PITSELs of different electrical series resistances. Curve 2 corresponds to the device reported in [9].

in Fig. 9. Due to nonlinear processes, the penalty for too high series resistance of the device increases rapidly with the pumping current. The operating current range of the 100-Ω device is therefore nearly twice smaller than that of the low-series-resistance (20 Ω) device (Fig. 10).

Figures 8 and 9 permit to estimate the range of validity of a simple linear treatment (dotted lines), in which R_{TH} is given by the uniform cylinder model. As one can see

in Fig. 8, the approximate model gives a very good estimate of R_{TH} near the lasing threshold. We can also see from Fig. 9 that a remarkably good agreement between approximate and exact active-region temperatures is obtained for low-series-resistance devices all the way up to 6 times the threshold current.

Evolution of the CW threshold current with pumping is shown in Fig. 10 for PITSELs with various series electrical resistances R_s. It should be emphasized that since the active-region temperature for a given device increases with the pumping current, the CW threshold also increases, even though the ambient temperature remains constant. When no direct current flows through the device (and, consequently, the active-region temperature is equal to the ambient temperature), the CW threshold can be considered to coincide with the pulsed threshold. A laser can operate CW if the thermally-induced increase in its CW threshold $I_{th,CW}$ is slower than the increase in the pumping current I. Hence, the lower intersection of the $I_{th,CW}$ curve (solid lines in Fig. 10) with the $I = I_{th,CW}$ line (dotted line) indicates the onset of CW lasing. However, as the pumping current is further increased, the CW threshold starts increasing superlinearly, and eventually thermal runaway takes place. The CW lasing action is no longer possible when the second intersection of the $I_{th,CW}$ curve with the $I = I_{th,CW}$ line is reached. Thus, Fig. 10 shows the entire CW operating range for each device.

6. Conclusions

A new comprehensive analytical thermal model of proton-implanted top-surface -emitting lasers presented in the first part of this paper has been applied to study thermal characteristics of GaAs/AlGaAs/AlAs devices with the active-region diameter of 35 μm [11]. Our results show that at high pumping currents a distinct thermal waveguiding effect focuses the laser radiation within the central parts of active regions. If integration of these devices into densely packed two-dimensional arrays were to be attempted long tails of radial temperature distribution will result in severe thermal crosstalk. Minimization of electrical series resistance is shown to be very important for improving the device performance. However, due to the p-side up mounting, calculated thermal resistance remains relatively large even when electrical series resistance is very small.

Acknowledgment – The work was supported by the Polish State Committee for Scientific Research (KBN), grants Nos. 7-T11B-069-20 and 7-T11B-073-21, and by the US-Poland Maria Skłodowska-Curie Fund No. MEN/NSF-98-336.

References

[1] TAYLOR E.W., PAXTON A.H., SCHONE H., CARSON R.F., BRISTOW J., LEHMAN J.A., HIBBS -BRENNER M.K., MORGAN R.A., MARTA T., IEEE Trans. Nucl. Sci. **45** (1997), 1514.
[2] WOODWARD T.K., HUNSCHE S., RITGER A.J., STARK J.B., IEEE Photon. Technol. Lett. **11** (1999), 382.
[3] FISCHER A.J., CHOQUETTE K.D., CHOW W.W., ALLERMAN A.A., GEIB K.M., Appl. Phys. Lett. **77** (2000), 3319.

[4] TAKAOKA K., ISHIKAWA M., HATAKOSHI G., *17th International Semiconductor Laser Conference*, September 25–28, 2000, p. 93.
[5] TANSU N., ZHOU D., RUSLI S., MAWST L.J., *12th IEEE Lasers and Electro-Optics Society Annual Meeteing*, LEOS'99, San Francisco, November 8–11, 1999, Vol. 2, p. 397.
[6] STARCK C., BOUCART J., PLAIS A., BOUCHE N., DEROUIN E., PINQUIER A., GABORIT F., BONNET -GAMARD J., FORTIN C., GOLDSTEIN L., BROLLOUET F., SALET P., CARPENTIER D., MARTINEAU M.-F., JACQUET J., *Conference on Lasers and Electro-Optics*, CLEO'99, May 23–25, 1999, p. 454.
[7] KAZIMIERSKI C., DEBRAY J.P., MADANI R., SAGNES J., OUGAZZADEN A., BOUADMA N., ETRILLARD J., ALEXANDRE F., QUILLEC M., Electron. Lett. **35** (1999), 811.
[8] MAĆKOWIAK P., SARZAŁA R.P., NAKWASKI W., *International Workshop on Nitride Semiconductors*, IWN 2000, Nagoya (Japan), September 24–27, 2000, [In] Proceedings, IPAP Conference Series **1** (2000), 889.
[9] ZHOU P., CHENG J., SCHAUS C.F., SUN S.Z., ZHENG K., ARMOUR E., HAINS C., HSIN W., MYERS D.R., VAWTER G.A., IEEE Photon. Techn. Lett. **3** (1991), 591.
[10] ZHOU P., CHENG J., SCHAUS C.F., SUN S.Z., HAINS C., ZHENG K., TORRES A., MYERS D.R., VAWTER G.A., Appl. Phys. Lett. **59** (1991), 2504.
[11] NAKWASKI W., MACKOWIAK P., OSINSKI M., Opt. Appl. **32** (2002), 157.
[12] HASNAIN G., TAI K., DUTTA N.K., WANG Y.H., WYNN J.D., WEIR B.E., CHO A.Y., Electron. Lett. **27** (1991), 915.
[13] NAKWASKI W., Opt. Quantum Electron. **28** (1996), 335.
[14] WOMAC J.F., REDIKER R.H., J. Appl. Phys. **43** (1972), 4129.
[15] LEE S.C., PEARSON G.L., J. Appl. Phys. **52** (1981), 5202.
[16] SOMMERS H.S., Jr., Appl. Phys. Lett. **19** (1971), 424.
[17] PAOLI T.L., IEEE J. Quantum Electron. **9** (1973), 267.
[18] GEELS R.S., CORZINE S.W., COLDREN L.A., IEEE J. Quantum Electron. **27** (1991), 1359.
[19] AMITH A., KUDMAN I., STEIGMEIER E.F., Phys. Rev. **138** (1965), A1270.
[20] ADACHI S., J. Appl. Phys. **54** (1983), 1844.
[21] TOULOUKIAN Y.S., POWELL R.W., HO C.Y., KLEMENS P.G., *Thermophysical Properties of Matter*, Vol. 1, *Thermal conductivity, Metallic Elements and Alloys*, IFI/Plenum, New York 1970.
[22] STRINGFELLOW G.B., J. Appl. Phys. **50** (1979), 4178.
[23] MUKAI S., MAKITA Y., GONDA S., J. Appl. Phys. **50** (1979), 1304.
[24] CHAND N., FISCHER R., KLEM J., HENDERSON T., PEARAH P., MASSELINK W.T., CHANG Y.C., MORKOÇ H., J. Vac. Sci. Technol. B **3** (1985), 644.
[25] SIGAI A.G., ABRAHAMS M.S., BLANC J., J. Electrochem. Soc. **119** (1971), 952.
[26] WILEY J.D., [In] *Semiconductors and Semimetals*, Vol. 10, *Transport Phenomena*, R.K. Willardson, A.C. Beer [Eds.], Academic Press, New York 1975, p. 91.
[27] LEE H.J., JURAVEL L.Y., WOOLLEY J.C., SPRINGTHORPE A.J., Phys. Rev. B **21** (1980), 659.
[28] MASU K., KONAGAI M., TAKAHASHI K., J. Appl. Phys. **51** (1980), 1060.
[29] SUN S.-Z., private communication.
[30] NAKWASKI W., KONTKIEWICZ A.M., IEEE Trans. Electron Dev. **32** (1985), 2282.
[31] NAKWASKI W., OSINSKI M., Electron. Lett. **28** (1992), 572, and Erratum **28** (1992), 1283.
[32] OSINSKI M., NAKWASKI W., IEEE J. Sel. Topics Quantum Electron. **1** (1995), 681.
[33] HASNAIN G., TAI K., WANG Y.H., FISCHER R.J., WYNN J.D., WEIR B., DUTTA N.K., CHO A.Y., IEEE J. Quantum Electron. **27** (1991), 1377.
[34] CHOQUETTE K.D., HASNAIN G., WANG Y.H., WYNN J.D., FREUND R.S., CHO A.Y., LEIBENGUTH R.E., IEEE Photon. Techn. Lett. **3** (1991), 859.
[35] COLDREN L.A., GEELS R.S., CORZINE S.W., SCOTT J.W., Opt. Quantum Electron. **24** (1992), 105.

Received March 18, 2002